Performance investigation and design optimization of a battery thermal management system with thermoelectric coolers and phase change materials

Ding Luo[a,b], Zihao Wu[a], Yuying Yan[d], Jin Cao[a], Xuelin Yang[a,*], Yulong Zhao[c,*], Bingyang Cao[b,*]

[a] College of Electrical Engineering & New Energy, China Three Gorges University, Yichang 443000, China

[b] Key Laboratory for Thermal Science and Power Engineering of Ministry of Education, Department of Engineering Mechanics, Tsinghua University, Beijing 100084, China

[c] Hebei Key Laboratory of Thermal Science and Energy Clean Utilization, Hebei University of Technology, Tianjin 300401, China

[d] Faculty of Engineering, University of Nottingham, University Park, Nottingham NG7 2RD, UK

Corresponding authors: *caoby@tsinghua.edu.cn (B. Cao); *zhaoyulong@hebut.edu.cn (Y. Zhao); *xlyang@ctgu.edu.cn (X. Yang)

Abstract: In this work, a novel battery thermal management system (BTMS) integrated with thermoelectric coolers (TECs) and phase change materials (PCMs) is developed to ensure the temperature working environment of batteries, where a fin framework is adopted to enhance the heat transfer. By establishing a transient thermal-electric-fluid multi-physics field numerical model, the thermal performance of the BTMS is thoroughly examined in two cases. The findings demonstrate that increasing the TEC input current, fin length, and thickness is beneficial for reducing the maximum temperature and PCM liquid fraction. Nevertheless, although the increase in fin length can lower the temperature difference, the influence of fin thickness and TEC input current on the temperature difference is tiny. Based on the numerical findings, the optimal fin length and thickness of 7 mm and 3 mm are obtained. In this situation, when the TEC input current is 3 A, the maximum temperature, temperature difference, and PCM liquid fraction in Case 1 are 315.10 K, 2.39 K, and 0.002, respectively, and those are respectively 318.24 K, 3.60 K, and 0.181 in Case 2. The configuration of Case 1 outperforms that of Case 2, due to the fewer TECs and greater distance from the battery pack to the TEC within Case 2. When experiencing a higher battery discharge rate, the TEC input current should also be correspondingly increased to ensure the temperature performance of the battery. The relative findings contribute to new insights into battery thermal management.

Keywords: thermoelectric; battery thermal management system; fin framework; numerical model; phase change material

Nomenclature

Symbols

c_p	specific heat, J·kg^{-1}·K^{-1}
d_h	hydraulic diameter, mm
$\vec{E}$	electric field density vector, V·m^{-2}
H	enthalpy, J·kg^{-1}
h	sensible heat enthalpy, J·kg^{-1}
Δh	phase change enthalpy, J·kg^{-1}
I	current, A
Re	Reynolds number
$\vec{J}$	current density vector, A·m^{-2}
k	turbulent kinetic energy, m^2·s^{-2}
L	fin length, mm
M	fin thickness, mm
p	pressure, Pa
Q	heat generation power, W
$\dot{S}$	source term
T	temperature, K
u	coolant flow speed, m/s
v	mass flow rate, kg·s^{-1}
V	volume, mm^3

Greek symbols

α	Seebeck coefficient, μV·K^{-1}
λ	thermal conductivity, W·m^{-1}·K^{-1}
γ	latent heat, J·kg^{-1}
ε	turbulent dissipation rate, m^2·s^{-3}
ρ	density, kg·m^{-3}
μ	dynamic viscosity, Pa·s
β	liquid fraction
σ	electrical conductivity, S·m^{-1}

Subscripts

b	battery
co	copper electrode
l	liquid phase
m	material
n	n-type thermoelectric leg
p	p-type thermoelectric leg
pcm	phase change material
s	solid phase

Abbreviations

BTMS	battery thermal management system
CFD	computational fluid dynamics
EV	electric vehicle
PCM	phase change material
PW	paraffin wax
TEC	thermoelectric cooler

1. Introduction

The vigorous promotion of electric vehicles (EVs), considered one of the key measures to reduce CO$_2$ emissions, has received strong support from the international community (Singh et al., 2023). Lithium-ion batteries, esteemed as the essential equipment in EV energy supply, have been highly commended for their exceptional characteristics of excellent energy density and cycle life (Shan et al., 2023; Weng et al., 2022). Nevertheless, achieving the high efficiency of lithium-ion batteries involves controlling their operating temperature within the range of 20-50°C and managing the overall temperature differential of the battery pack to a value below 5°C (Lin and Zhou, 2023). Nonetheless, in practical operation, the electrochemical reactions occurring within lithium-ion batteries give rise to significant high-temperature issues (Subramanian et al., 2021). In the absence of effective cooling measures, the possibility of thermal runaway in batteries exists, which can ultimately lead to the spontaneous combustion of EVs (Liu et al., 2023). Hence, there is a pressing demand for the innovation of an effective battery thermal management system (BTMS) to resolve the high-temperature concern in lithium-ion batteries.

In the field of BTMS, liquid cooling, air cooling, thermoelectric cooler (TEC) cooling, heat pipe cooling, and phase change material (PCM) cooling are the predominant technical methodologies (Mousavi et al., 2023). Leveraging the high latent heat properties of PCMs, the PCM-based BTMS can effectively govern the battery temperature while ensuring temperature uniformity without necessitating any additional energy consumption (Luo, J. et al., 2023). Nevertheless, the application of PCMs in battery thermal management presents a formidable challenge due to their low thermal conductivity and restricted latent heat. For this reason, many researchers have tried to improve the thermal conductivity of PCMs (Ling et al., 2021; Subramanian et al., 2021). Li et al. (2014) conducted a dedicated experiment to assess the effect of incorporating the porous metal foam into the pure PW-based PCM on the dissipation of battery heat; They found that the utilization of composite PCMs contributes to further reducing the battery temperature. Talele and Zhao (2023) employed a numerical simulation to investigate the impact of nano-enhanced PCMs, composed of pure PW-based PCMs and alumina nanoparticles, on battery heat dissipation; It was revealed that the utilization of the nano-enhanced PCM facilitates battery heat conduction and temperature control. The mentioned research offers an effective solution to improve the thermal conductivity of PCMs.

Nonetheless, the introduction of high thermal conductivity materials undoubtedly lowers the latent heat of PCMs. Once the PCM's latent heat is completely consumed, it may cause serious heat accumulation problems within the battery pack, thereby increasing the risk of thermal runaway of the battery. Meanwhile, the temperature difference across the battery pack rises rapidly. Hence, the coupling of PCMs with air or liquid cooling-based BTMS has become a mainstream research direction (Zhang et al., 2021; Zhang, Y. et al., 2022). Ranjbaran et al. (2023) numerically studied the effects of cooling duct shape and inlet pressure on the thermal performance of a BTMS that incorporates PCMs and air cooling; The results indicated that the system maintains effective control over the maximum battery temperature and temperature difference, even under the demanding conditions. Yang et al. (2023) employed a numerical simulation to investigate the performance of a BTMS that combines a Z-shaped liquid cooling plate and PCM/foam aluminum; They found that this combination could efficiently reduce the energy consumption of the system while upholding proficient heat dissipation. However, the integration of air or liquid cooling with PCMs still holds limitations. Air cooling is hard to reach the internal region of PCMs, while liquid cooling technology is limited by its size, weight, and substantial power usage (Babu Sanker and Baby, 2022). Therefore, it is necessary to find an efficient cooling and environmentally friendly technology to combine with PCMs.

Thermoelectric cooling, as an emerging active battery thermal management technology, is leading a new trend in the field of battery thermal management with unique advantages such as fast response, no emissions, efficient cooling, precise temperature control, and flexible switching of dissipation or preheating modes (Sait, 2022). Nevertheless, the operation of the TEC demands a continuous current input, leading to significant power consumption in the TEC-based BTMS. Consequently, integrating the TEC-based active BTMS with the PCM-based passive BTMS presents a practical solution (Siddique et al., 2018). Jiang et al. (2019) used a combination of experiments and numerical simulations to study the performance of a BTMS integrating with copper foam composite PCMs and TECs; Their outcomes demonstrated a substantial decrease in the maximum battery temperature and a significant prolongation of lifespan in contrast to the natural air convection and liquid cooling method. Liu et al. (2022) utilized a numerical simulation to analyze the effectiveness of a BTMS combining PCMs and TECs; Their research revealed that as the TEC input current is increased, there is a substantial decrease in battery temperature, but this comes at the expense of declining temperature uniformity and coefficient of performance. Song et al. (2018) designed a BTMS based on the TEC and PCMs for prismatic batteries, and analyzed its thermal performance under different charging and discharging rates by CFD simulations; Their results showed that the battery temperature could meet the requirements for the majority of the time, both in the cooling and heating processes. However, the reported BTMS integrated with TECs and PCMs is limited by the low thermal conductivity of PCMs. During the high-rate battery discharge process, the PCM experiences excessive melting, causing a rapid rise in battery temperature and temperature difference, surpassing predefined limits. Meanwhile, for the BTMS coupled with TECs and PCMs, the current performance investigation mainly relies on the CFD (Computational Fluid Dynamics) simulation or heat transfer modeling, lacking systematic analysis and failing to consider multi-physics coupling characteristics.

Accordingly, this work proposes a novel BTMS that combines PCMs and TECs, in which a fin framework is introduced to enhance the heat transfer from the TEC to the battery and PCMs. The fin framework structure enables the TEC to efficiently control the PCM melting and battery temperature. In addition, the design of stacked structures has the potential for extensive expansion, which is conducive to the widespread application of the system. Regarding the numerical modeling aspect, a transient thermal-electric-fluid multi-physics field numerical model is developed to evaluate the thermal performance of the proposed BTMS. On this basis, comprehensive performance investigations and design optimizations for the BTMS are conducted, including exploring the effects of various parameters on the BTMS thermal performance, i.e., structural configuration, fin length and thickness, TEC input current, and discharge rate.

2. Geometric description of the novel BTMS

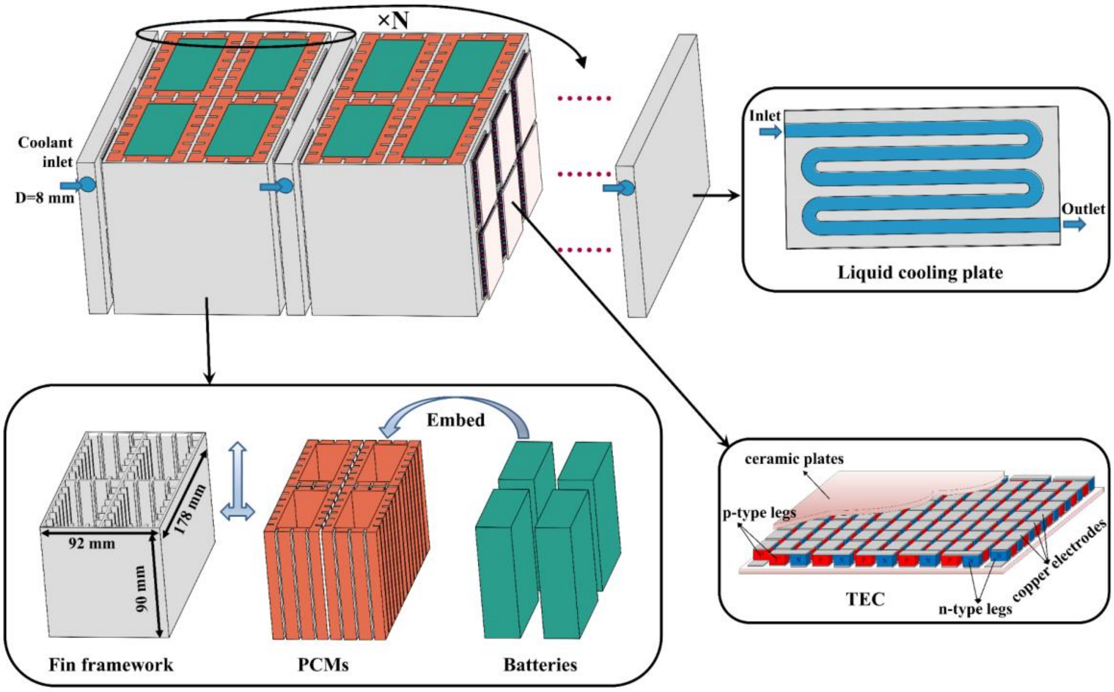

Fig. 1. Schematic diagram of the three-dimensional geometry of the BTMS.

Fig. 1 presents a schematic diagram of the geometric model for the novel BTMS proposed in this work. The system comprises *N* identical cells, with a shared S-shaped liquid cooling plate positioned between adjacent cells. Notably, both sides of the liquid cooling plate feature an identical distribution of TECs. Building upon the mentioned design, the proposed novel BTMS incorporates a stacked structure, endowing it with unlimited scalability and significantly boosting its suitability for diverse practical scenarios. In order to present a visual depiction of the geometry of the BTMS, a representative cell is selected for an elaborate description. The cell comprises the battery pack, the pure PW-based PCM, the aluminum fin framework, the TEC, and the S-shaped liquid cooling plate. The aluminum fin framework encompasses the outer framework, inner partitions, and fins, with dimensions (length × width × height) of 178 mm × 92 mm × 90 mm and a thickness of 2 mm. The central cavity of the outer framework is divided into four small rectangular cavities with equal sizes through horizontal and vertical partitions. Additionally, rectangular fins with uniform sizes are evenly distributed on both the outer framework and inner partitions to enhance heat transfer efficiency. The four prismatic $LiFeO_4$ batteries in the battery pack are ingeniously positioned at the central region of the four small cavities.

The space remaining between these small cavities and batteries is appropriately filled with pure PW-based PCMs. The same number and size of TECs are uniformly placed on both sides of the outer framework. The TEC incorporates p/n-type thermoelectric legs, copper electrodes, and ceramic plates. Upon supplying power to the TEC, the ceramic plate at one end undergoes heating and operates as the heating side, while the ceramic plate at the other end concurrently cools down, functioning as the cooling side. The cooling end is tightly affixed to the outer framework, delivering a cooling source to the battery pack and PCM, while the heating end is interconnected with the S-shaped liquid cooling plate, through which the temperature of the heating end is reduced to enhance the cooling efficiency of TECs. The S-shaped liquid cooling plate has a thickness of 10 mm, and the internal liquid flow channel has a diameter of 8 mm. Water is selected as the cooling medium within the flow channel. Further geometric information can be referred to in Fig. 1.

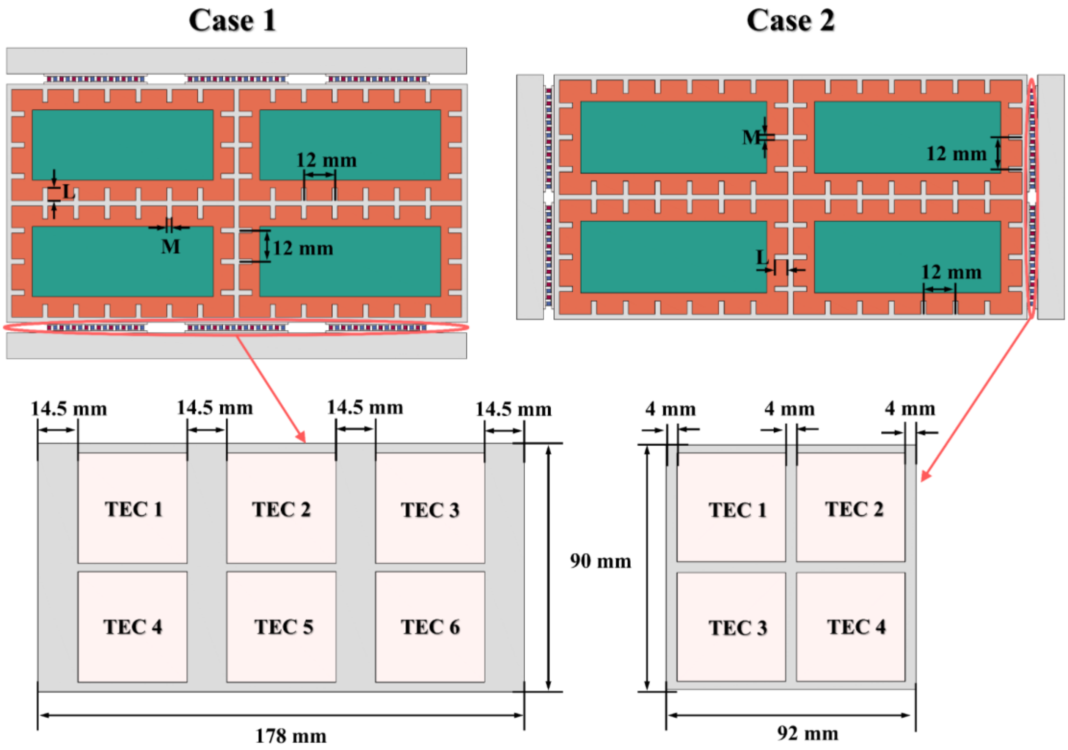

Fig. 2. Geometry of the system and arrangement of the TEC in different cases.

In addition, the above description demonstrates that the stacked-based system structure still holds in the case of mounting the TEC on the other two sides of the aluminum fin framework. The geometry of the system and the arrangement of TECs for different cases are illustrated in Fig. 2. In Case 1, there is a uniform distribution of TECs on both the front and rear exterior surfaces of the aluminum fin outer framework, comprising 6 TECs per exterior surface. In Case 2, the left and right exterior surfaces of the aluminum fin outer framework showcase a similar uniform arrangement, with 4 TECs affixed to each exterior surface. Notably, in Case 1, the length of the S-shaped liquid cooling plate is set at 178 mm, whereas in Case 2, it is adjusted to 92 mm, ensuring an exact match with the dimensions of the outer framework. Table 1 presents the material parameters of the battery (Liu et al., 2022), aluminum, water, and pure PW-based PCM (Zhang, F. et al., 2022). To access detailed information regarding the dimensions and material parameters of the TEC components, kindly refer to Table 2 (Hu et al., 2023).

Table 1. Material parameters for battery (Liu et al., 2022) and other components (Zhang, F. et al., 2022).

Component	Specific heat ($J \cdot kg^{-1} \cdot K^{-1}$)	Density ($kg \cdot m^{-3}$)	Thermal conductivity ($W \cdot m^{-1} \cdot K^{-1}$)	latent heat ($J \cdot kg^{-1}$)	Phase change temperature (K)
Aluminum	900	2700	238	-	-
Battery	1150	1838.2	x, y: 15.3 z: 0.9	-	-
PCM	2000	800	0.2	255000	314.15-317.15
Water	4200	998	0.6	-	-

Table 2. Dimensions and material parameters of each component of the TEC (Hu et al., 2023).

	Seebeck coefficient ($\mu V \cdot K^{-1}$)	Thermal conductivity ($W \cdot m^{-1} \cdot K^{-1}$)	Electrical conductivity ($S \cdot m^{-1}$)	Size ($L \times W \times H$ mm^3)
p-type legs	$-1.593\times10^{-9}T^2+1.364\times10^{-6}T$ -7.062×10^{-5}	$1.071\times10^{-5}T^2-8.295\times10^{-3}T$ $+2.625$	$1.311T^2-1.364\times10^3T$ $+4.023\times10^5$	1.4 × 1.4 × 1.6
n-type legs	$7.393\times10^{-11}T^2-2.500\times10^{-7}T$ -8.494×10^{-5}	$1.870\times10^{-5}T^2-1.447\times10^{-2}T$ $+3.680$	$0.657T^2-7.136\times10^2T$ $+2.463\times10^5$	1.4 × 1.4 × 1.6
copper electrodes	-	400	5.998×10^7	3.8 × 1.4 × 0.4
ceramic plates	-	22	-	40 × 40 × 0.8

3. The transient thermal-electric-fluid multi-physical field numerical model

3.1 Model hypothesis

Before building a numerical model, some necessary model hypotheses need to be made explicit:

(i) The material characteristics of both the battery and PCM remain constant and unaffected by temperature fluctuations (Li, B. et al., 2023).

(ii) The volume of PCMs is constant when they undergo the melting process.

(iii) Heat generation inside the battery occurs evenly and spreads out in all orientations (Liu et al., 2022).

(iv) Neglecting the effect of convective heat transfer after melting of the PCM (Cao et al., 2020).

(v) The effect of thermal radiation is not considered (Luo, D. et al., 2023d).

3.2 Governing equations

Within the numerical model for transient thermal-electric-fluid multi-physics, the governing equations can be segregated into three components: solid domains other than the TEC, the TEC domain, and the fluid domain.

3.2.1 Governing equations for solid domains other than the TEC

For this work, the prismatic $LiFeO_4$ battery is utilized, with dimensions of 70 mm × 27 mm × 90 mm (length × width × height) and a nominal capacity of 12 Ah (Wu et al., 2018). Heat generation inside the battery can be controlled using the following energy conservation equation:

$$\frac{\partial}{\partial t}(\rho_{\mathrm{b}} c_{p,\mathrm{b}} T_{\mathrm{b}}) = \nabla \cdot (\lambda_{\mathrm{b}} \nabla T_{\mathrm{b}}) + \frac{Q_{\mathrm{b}}}{V_{\mathrm{b}}} \tag{1}$$

where T, t, ρ, λ, and c_p denote temperature, time, density, thermal conductivity, and specific heat, respectively, the subscript b represents the battery, and V_{b} and Q_{b} are the volume and heat generation power, respectively. The battery discharge rate can be quantified using the C-rate, which represents the operating current relative to the nominal current. For instance, a discharge rate of 3 C indicates that the battery operates with a current three times higher than its nominal current of 12 A. Table 3 presents the heat generation power of the battery at various discharge rates, according to the reference value in (Wu et al., 2018) and the method in (Heyhat et al., 2020).

Table 3. Heat generation power of batteries under different discharge rates (Wu et al., 2018; Heyhat et al., 2020).

Discharge rate (C)	3	4	5
Heat generation power (W)	12.96	17.28	21.60

The heat conduction mechanism within the PCM can be modeled using the enthalpy method, and its corresponding governing equation is expressed as follows (Zhang et al., 2023):

$$\rho_{\mathrm{pcm}} \frac{\partial H_{\mathrm{pcm}}}{\partial t} = \lambda_{\mathrm{pcm}} \nabla^2 T_{\mathrm{pcm}} \tag{2}$$

$$H_{\mathrm{pcm}} = h + \Delta h \tag{3}$$

$$h = \int_{T_0}^{T_{\mathrm{pcm}}} c_{p,\mathrm{pcm}} dT_{\mathrm{pcm}} \tag{4}$$

$$\Delta h = \beta \gamma \tag{5}$$

where H_{pcm}, h, Δh, and γ are the enthalpy, sensible heat enthalpy, phase change enthalpy, and latent heat of the PCM, respectively, the subscript pcm represents the pure PW-based PCM, and the specific value of the liquid fraction β of the PCM can be defined using the following segmental function (Peng et al., 2022):

$$\beta = \begin{cases} 0 T_{\mathrm{pcm}} < T_{\mathrm{s}} \\ \dfrac{T_{\mathrm{pcm}} - T_{\mathrm{s}}}{T_{\mathrm{l}} - T_{\mathrm{s}}} T_{\mathrm{l}} < T_{\mathrm{pcm}} < T_{\mathrm{s}} \\ 1 T_{\mathrm{pcm}} > T_{\mathrm{l}} \end{cases} \tag{6}$$

where T_{s} and T_{l} are the initial melting temperature and complete melting temperature of the PCM, respectively.

The energy conservation equation for the solid aluminum portion of the fin framework and the S-shaped liquid cooling plate can be characterized by:

$$\frac{\partial}{\partial t}(\rho c_p T) = \nabla \cdot (\lambda \nabla T) \tag{7}$$

3.2.2 Governing equations of the TEC domain

The governing equation of the TEC domain can be split into two parts: the heat conduction domain and the electric field domain. Within the heat conduction domain, ceramic plates, copper electrodes, and p/n type thermoelectric legs are subject to the following energy conservation equations (Luo, D. et al., 2023c):

$$\frac{\partial}{\partial t}(\rho_{\mathrm{m}} c_{p,\mathrm{m}} T_{\mathrm{m}}) = \nabla \cdot (\lambda_{\mathrm{m}} \nabla T_{\mathrm{m}}) + \dot{S}_{\mathrm{m}} \tag{8}$$

where $\dot{S}$ is the energy source term, and the subscript m denotes the material of each component of the thermoelectric cooler. As the electric current flows through both the p/n-type thermoelectric leg and the copper conductor, it results in the generation of Joule heat. Simultaneously, Peltier heat and Thomson heat are also produced within the p/n-type thermoelectric leg (Tang et al., 2023). The specific expression for $\dot{S}_{\mathrm{m}}$ is as follows (Luo, D. et al., 2023c):

$$\dot{S}_{\mathrm{m}} = \begin{cases} \sigma_{\mathrm{p}}^{-1}(T)\vec{J}^{2} - T_{\mathrm{p}}\vec{J}^{-1} \cdot \nabla\alpha_{\mathrm{p}}(T) - \dfrac{\partial\alpha_{\mathrm{p}}(T)}{\partial T} T\vec{J} \cdot \nabla T_{\mathrm{p}}; & \text{p-type thermoelectric leg (9-1)} \\ \sigma_{\mathrm{n}}^{-1}(T)\vec{J}^{2} - T_{\mathrm{n}}\vec{J}^{-1} \cdot \nabla\alpha_{\mathrm{n}}(T) - \dfrac{\partial\alpha_{\mathrm{n}}(T)}{\partial T} T\vec{J} \cdot \nabla T_{\mathrm{n}}; & \text{n-type thermoelectric leg (9-2)} \\ \sigma_{\mathrm{co}}^{-1}(T)\vec{J}^{2}; & \text{copper electrode (9-3)} \\ 0; & \text{ceramic (9-4)} \end{cases} \tag{9}$$

where $\vec{J}$, σ^{-1}, and α denote the current density vector, electrical resistivity, and Seebeck coefficient, respectively. The subscripts co, p, and n represent the copper electrode, p-type thermoelectric leg, and n-type thermoelectric leg, respectively. For p/n type thermoelectric legs, the terms in Eqs (9-1) and (9-2) from left to right represent Joule heat, Peltier heat, and Thomson heat, respectively (Luo, D. et al., 2023a).

The electric field conservation equations are used for characterizing p-type thermoelectric legs, n-type thermoelectric legs, and copper electrodes of the TEC within the electric field domain (Luo, D. et al., 2023d):

$$\vec{E} = -\nabla\phi + \alpha_{\mathrm{p,\,n}}(T)\nabla T \tag{10}$$

$$\vec{J} = \sigma_{\mathrm{m}}\vec{E} \tag{11}$$

$$\nabla\cdot\vec{J} = 0 \tag{12}$$

where $\vec{E}$ and ϕ denotes the electric field vector density and the electric potential, respectively.

3.2.3 Governing equations of the fluid domain

Utilizing the following transient computational fluid dynamics equations to characterize the fluid domain of the cooling medium inside the S-shaped liquid cooling plate (Luo, D. et al., 2023b):

$$\frac{\partial}{\partial t}\left(\rho c_p T\right) + \nabla\cdot\left(\rho c_p \vec{v} T\right) = \nabla\left(\lambda\nabla T\right) \tag{13}$$

$$\frac{\partial}{\partial t}(\rho\vec{v}) + \nabla\cdot\left(\rho\vec{v}\vec{v}\right) = -\nabla p + \nabla\cdot(\mu\nabla\vec{v}) \tag{14}$$

$$\frac{\partial\rho}{\partial t} + \nabla\cdot\left(\rho\vec{v}\right) = 0 \tag{15}$$

where μ, p, and $\vec{v}$ denote the dynamic viscosity, pressure, and velocity vectors, respectively. Eqs. (13)-(15) represent the energy conservation, momentum conservation, and mass conservation equations for the transient state, respectively. The determination of the specific flow pattern of the coolant depends on the Reynolds number, which can be determined using the following equation:

$$Re = \frac{u \times d_{\mathrm{h}}}{\mu} \tag{16}$$

where u and d_{h} are the coolant flow speed and the hydraulic diameter of the channel, respectively. The coolant flow rate is fixed as 0.01 kg/s herein, resulting in a calculated Reynolds number of 3360, which surpasses 2300. Consequently, the simulations in this work adopt the realizable k-ε turbulence model (Li, M. et al., 2023), which transport equations include:

$$\rho\frac{\partial k}{\partial \mathrm{t}} + \rho(\vec{v}\cdot\nabla)k = \nabla\cdot\left[\left(\mu + \frac{\mu_{\mathrm{T}}}{\sigma_{\mathrm{k}}}\right)\nabla k\right] + p_{\mathrm{k}} - \rho\varepsilon \tag{17}$$

$$\rho\frac{\partial\varepsilon}{\partial \mathrm{t}}+\rho(\vec{v}\cdot\nabla)\varepsilon=\nabla\cdot\left[\left(\mu+\frac{\mu_{\mathrm{T}}}{\sigma_{\varepsilon}}\right)\nabla\varepsilon\right]+C_1\rho S\varepsilon-C_{\varepsilon 2}\frac{\rho\varepsilon^2}{k+\sqrt{v_1\varepsilon}} \tag{18}$$

with

$$C_1=max\left\{0.43,\frac{\eta}{5+\eta}\right\},\eta=\frac{Sk}{\varepsilon} \tag{19}$$

$$\mu_{\mathrm{T}}=\rho C_{\mu}\frac{k^2}{\varepsilon},C_{\mu}=\frac{1}{A_0+A_{\mathrm{s}}\frac{k}{\varepsilon}U^*} \tag{20}$$

where k, p_{k}, and ε are the turbulence kinetic energy, shear production of turbulence kinetic energy, and turbulence kinetic energy dissipation rate, respectively, and the values of the model constants $C_{\varepsilon 2}$, σ_{k}, σ_{ε}, and A_0 are 1.9, 1.0, 1.2 and 4.0, respectively. The specific parameters information can be found in Ref. (Fu et al., 2016).

Eqs (1)-(20) mentioned above are basic governing equations of the transient thermal-electric-fluid multi-physical field. Commonly used numerical computational methods for solving these differential equations include the finite volume, finite element, and finite difference methods (Luo, D. et al., 2023c). In this work, the backward difference method is used for the discretization of the time variable, and the finite element method is chosen for discretizing the space variables.

3.3 Boundary conditions of the numerical model

Based on the commercial software COMSOL, numerical simulations of the aforementioned transient thermal-electric-fluid multi-physical field numerical model are performed. The simulation starts at 0 s with a time step of 0.5 s, and the initial temperature is set as 303.15 K, corresponding to the ambient temperature. A discharge time of 270 min is selected in this work, to explore whether the battery temperature, temperature difference, and PCM melting exceed the limits when the system reaches a stable state after multiple charging and discharging cycles. For the TEC, the copper electrode located at the current inflow end is specified as the terminal, with the copper electrode at the current outflow end designated as the ground. For the S-shaped liquid cooling plate, set inlet boundary conditions on the surface where the cooling medium enters, with a mass flow rate set at 0.01 kg/s and an inlet temperature of 303.15 K. Meanwhile, the outlet surface of the cooling medium is treated with a standard atmospheric pressure as the outlet boundary condition. Assign heat loss boundary conditions to the surfaces of the BTMS exposed to the external environment, with a natural convection heat transfer coefficient specified as 5 W·m^{-2}·K^{-1}.

3.4 Grid independence examination

Finer grid size is helpful to enhance calculation precision but is accompanied by a notable increase in computational time. Therefore, conducting a grid independence examination is essential to strike the optimal balance between accuracy and computational efficiency. The grid independence analysis conducted in this work is based on Case 1, utilizing four grid numbers with a gradual increase: 491575, 861504, 1648287, and 2436493. Before initiating the grid independence examination, it is essential to set the simulation conditions, comprising a battery discharge rate of 3 C, a TEC operating current of 3 A, and fin length and thickness of 5 mm and 2 mm, respectively. The variation of the maximum temperature with time for different grid numbers is showcased in Fig. 3(a). When the grid number hits 1648287, the results demonstrate that the maximum temperature closely approximates that of 2436493 grids, with negligible deviation. Therefore, to achieve a compromise between computational precision and time consumption, a grid number of 1648287 is chosen in this work. Fig. 3(b) gives specific grid details of the BTMS at this chosen grid number.

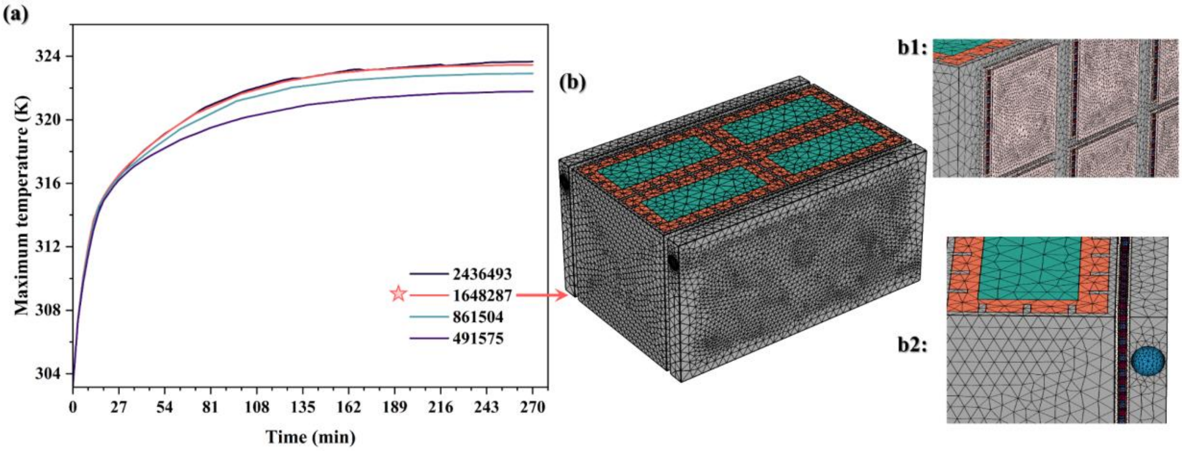

Fig. 3. (a) Maximum temperature of the battery pack for different grid numbers; (b) Details of the grid distribution.

3.5 Experimental validation

To verify the accuracy of the developed transient thermal-electric-fluid multi-physics field numerical model, experimental data from previously published literature is compared with the model results in this work. Firstly, a three-dimensional geometric model of the BTMS in Ref. (Jiang et al., 2019) is established, which integrates TECs and PCMs. Then, a finite element model for the BTMS is built and its performance is predicted by the transient thermal-electric-fluid multi-physics field numerical model. During numerical simulations, the boundary conditions are consistent with the experimental conditions in Ref. (Jiang et al., 2019), to avoid deviations in the results caused by other factors. Fig. 4 illustrates a comparison of the maximum temperature between the experimental data in published literature and the simulation results in this work. It can be observed that the simulation results are in good agreement with the experimental data, with an average deviation of about 0.92 K within 7200 s. This tiny deviation indicates that the transient thermal-electric-fluid multi-physics field numerical model can be used to precisely evaluate the thermal performance of the BTMS, which further highlights the reasonability and credibility of the following results.

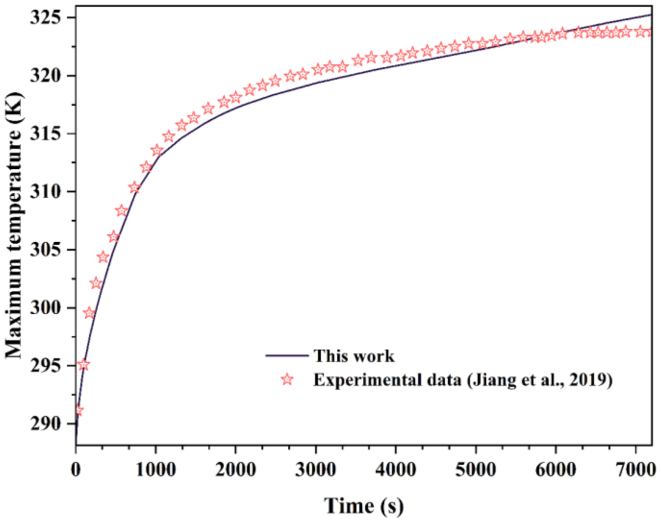

Fig. 4. Comparison of the maximum temperature between numerical results and experimental results.

4. Results and discussion

This work assesses the thermal performance of the BTMS by considering key indicators such as the maximum temperature and temperature difference of the battery pack and the liquid fraction of the PCM. Specifically, the maximum temperature is defined as the maximum temperature on the surface of all batteries, and the maximum temperature difference is derived from the difference between the maximum and minimum temperatures among different batteries. Also, the liquid fraction of the PCM is calculated by Eq. (6).

4.1 Overall description of the BTMS simulation results

The temperature distribution of the complete BTMS and the battery pack, as well as the liquid fraction distribution of the PCM for both cases, are shown in Fig. 5. The simulation conditions used herein are the same as those used in the grid independence examination. Fig. 5(a) illustrates the overall temperature distribution contour of the BTMS. In Case 1, the system displays a lower overall temperature than in Case 2. Additionally, in Case 2, both the fin framework and the PCM in the middle part indicate substantially higher temperatures compared to Case 1. Fig. 5(b) exhibits the temperature distribution contour of the battery pack in both cases. Observably, Case 2 indicates a larger high-temperature area and less temperature uniformity. The difference between Case 1 and Case 2 can be attributed to the variation in the TEC arrangement. In Case 1, six TECs are placed on both the front and rear of the fin framework, with a shorter distance between TECs on each side. As a result, this configuration enhances the cooling efficiency of the battery and PCM. Fig. 5(c) illustrates the liquid fraction contour of the PCM in both cases. Specifically, in Case 1, only the PCM in direct contact with the battery is melted, while in Case 2, a larger part of the PCM located in the central region has undergone melting. This difference can be attributed to the higher heat accumulation in the central region of the PCM in Case 2. Additionally, the temperature distribution contour of batteries depicted in Fig. 5(b) showcases that the maximum temperature in Case 2 is already higher than the limitation of 323.15 K based on the given initial conditions. Thus, further optimization of the proposed BTMS is required in subsequent investigations.

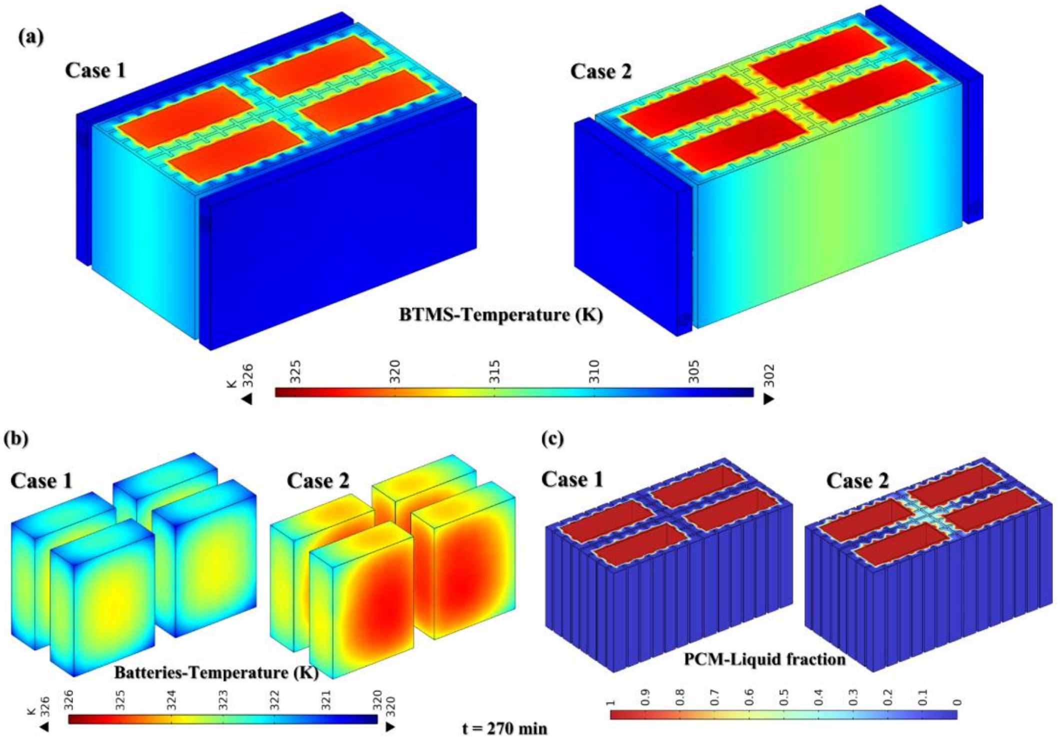

Fig. 5. Numerical results of the BTMS. (a) Temperature distribution contours of the complete BTMS; (b) Temperature distribution contours of the battery pack; (c) Liquid fraction distribution contours of PCMs.

4.2 Effect of fin length

The heat transfer efficiency among the TEC, PCM, and battery is mainly contingent on the dimensions of the fin framework, especially the fin length and thickness. In this work, the fin length is first optimized. Once the optimal fin length is determined, we proceed to optimize the fin thickness.

Considering that the thickness of the PCM is 8 mm, various fin lengths (1 mm, 3 mm, 5 mm, 7 mm) not exceeding 8 mm are selected for optimizations while maintaining the discharge rate, TEC input current, and fin thickness constant at 3 C, 3 A, and 2 mm, respectively.

Figs 6(a) and 6(b) display variations in maximum temperature and temperature difference, respectively. It is clear that for both cases, an increase in fin length leads to a decrease in both the maximum temperature and temperature difference of batteries. Specifically, as the fin length increases from 1 mm to 7 mm, the maximum temperature decreases from 334.35 K to 315.85 K for Case 1, along with a reduction in the temperature difference from 4.14 K to 2.39 K. Correspondingly, in Case 2, the maximum temperature decreases from 335.99 K to 318.65 K, and the temperature difference decreases from 4.60 K to 3.42 K. The primary cause is that elongating the fin length diminishes the distance between the fin framework and battery pack, concurrently augmenting the contact area between the aluminum fin framework and PCM. Consequently, this enhances the heat transfer among the TEC, PCM, and battery.

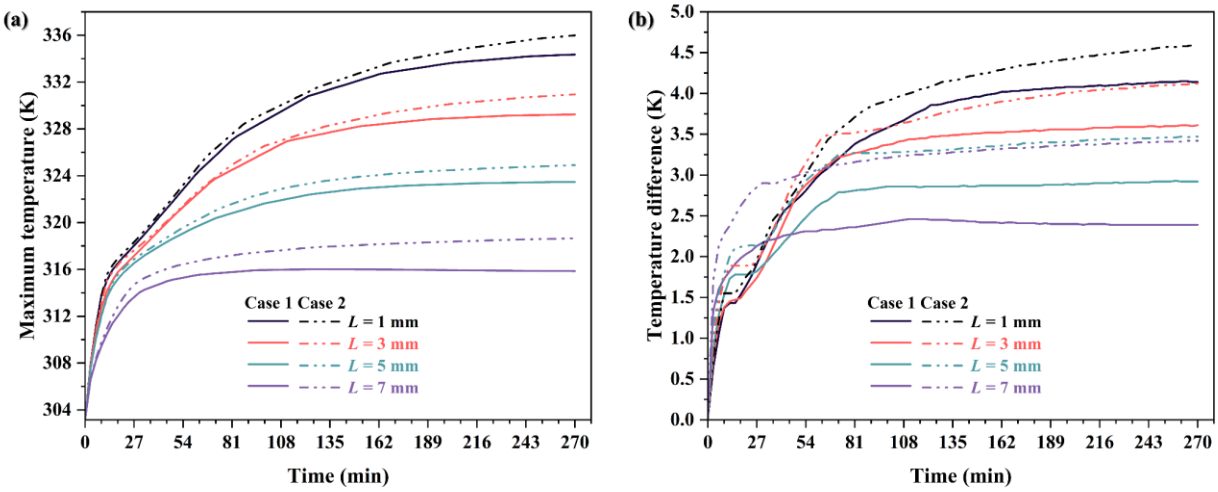

Fig. 6. Effect of fin length. (a) Maximum temperature; (b) Temperature difference

According to Fig. 6(b), it is worth noting that for fin lengths less than 7 mm, the maximum battery temperature difference exhibits distinct phases of rapid increase, stabilization, followed by a rapid increase, and eventual leveling off. However, with a fin length of 7 mm, the temperature difference experiences a rapid increase and then stabilization. The primary cause is that with a fin length below 7 mm, during the initial phase of battery discharge, the maximum temperature remains below the melting point of PCMs, resulting in a rapid increase in the maximum temperature and temperature difference. However, when the maximum temperature reaches the melting point, the rate of increase in the temperature difference slows down. With the discharge proceeding, the PCM begins melting, resulting in a reduction in its ability to control temperature and a rapid increase in the temperature difference between batteries. As the PCM melts further, both the maximum temperature and temperature difference tend to stabilize. Nevertheless, with a fin length of 7 mm, it becomes evident that the PCM remains largely unmelted, resulting in the temperature difference going through a mere rapid increase phase followed by stabilization.

Fig. 7 shows the battery pack temperature distribution contours at 270 min. It is evident that increasing the fin length can effectively lower the maximum battery temperature and high-temperature range in both Case 1 and Case 2. Additionally, the battery surface temperature closer to the TEC shows a more pronounced decrease with the increase in fin length.

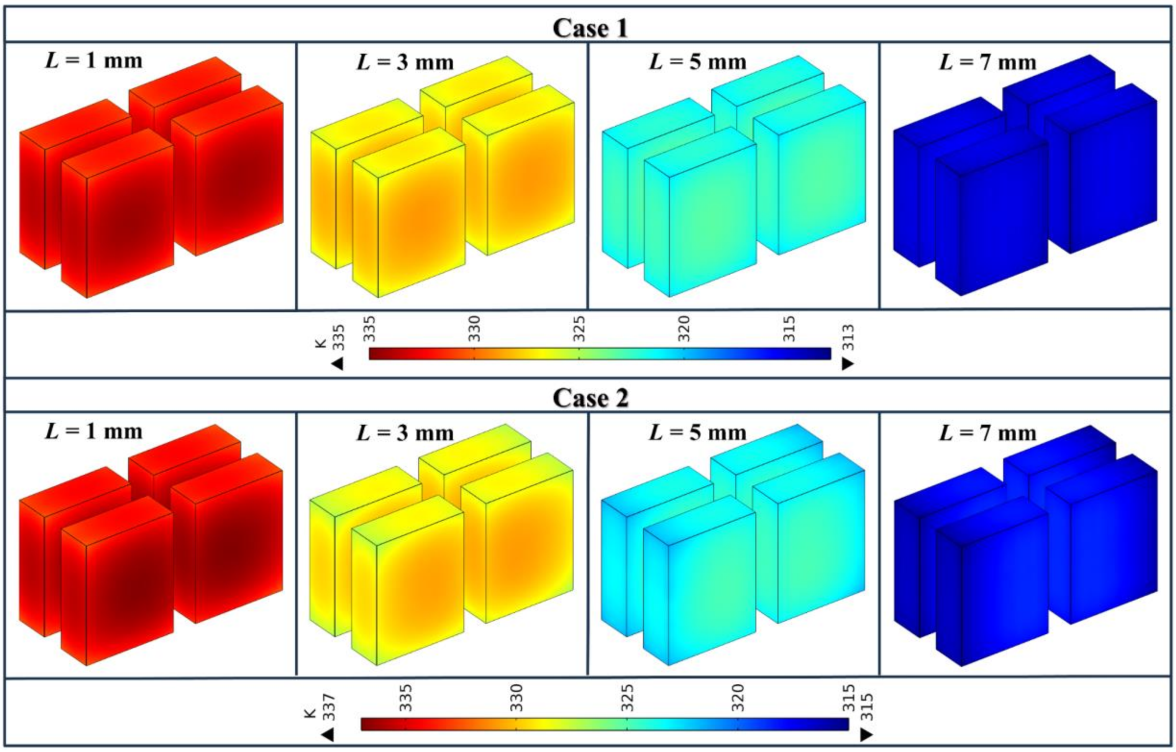

Fig. 7. Contours of the battery pack temperature distribution under different fin lengths at 270 min.

The liquid fraction of PCMs under different fin lengths is showcased in Fig. 8(a). It is evident that during the initial phase of battery discharge, the PCM does not undergo melting. However, as the discharge time progresses, there is a rapid rise in the liquid fraction, which subsequently reaches a steady level. Combined with Fig. 6(a), it is observable that as the discharge commences, the maximum battery temperature remains under the melting point of PCMs, thus, the PCM does not melt. Once the maximum temperature attains the melting point of PCMs, the PCM undergoes melting, resulting in a rapid rise of its liquid fraction. Eventually, as the discharge progresses, the PCM liquid fraction stabilizes. Increasing the fin length results in a decrease in the liquid fraction of PCMs in both cases. When the fin length is extended from 1 mm to 7 mm, the liquid fraction of PCMs decreases by 0.636

for Case 1 and by 0.523 for Case 2. The liquid fraction distribution contour of PCMs at 270 min is showcased in Fig. 8(b). At a fin length of 1 mm, the PCM adjacent to the battery pack undergoes complete melting in both cases, with Case 2 exhibiting additional melting in the middle portion of the PCM compared to Case 1. With an increase in fin length to 7 mm, the PCM melting does not occur in Case 1, but in Case 2, the region directly touching the battery starts to melt.

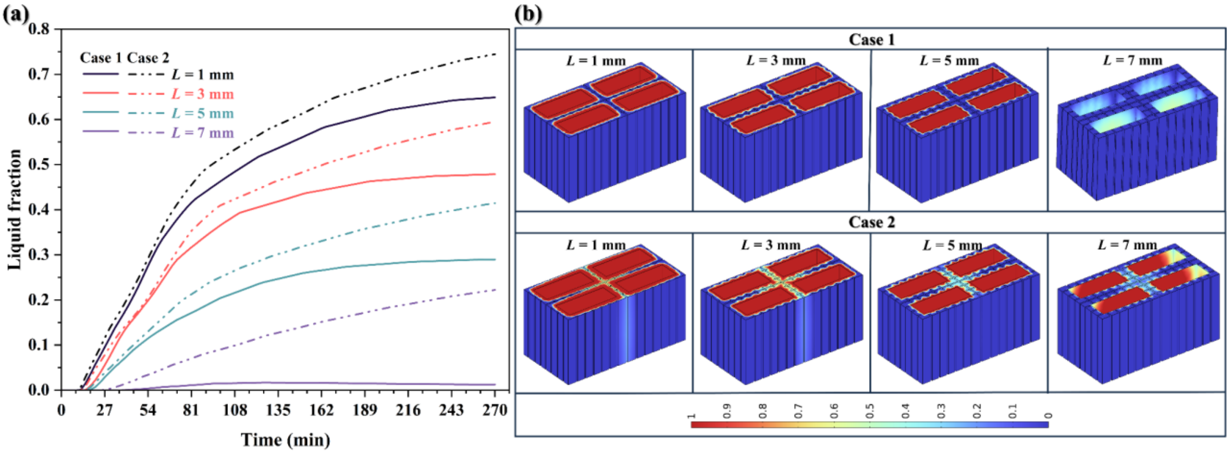

Fig. 8. Liquid fraction of PCMs at different fin lengths. (a) The change of liquid fraction of PCMs during battery discharge; (b) Liquid fraction distribution contours of PCMs at 270 min.

In summary, the greater the fin length, the better the thermal performance of the BTMS. Considering the geometric limitation, the optimal fin length of 7 mm is suggested.

4.3 Effect of fin thickness

Apart from the fin length, the fin thickness is another crucial factor influencing the thermal performance of the BTMS. Investigations are conducted with fin thickness ranging from 1 mm to 4 mm, while maintaining the fin length, TEC input current, and discharge rate remain constant at 7 mm, 3 A, and 3 C, respectively.

Figs 9(a) and 9(b) illustrate the variation of maximum temperature and temperature difference under different fin thicknesses. Increasing the fin thickness increases the heat transfer area among the fin and PCM, decreasing the maximum battery temperature for both cases. Specifically, when the fin thickness is increased from 1 mm to 4 mm, the maximum temperature decreases from 316.69 K to 314.50 K for Case 1 and from 319.30 K to 317.67 K for Case 2. However, the temperature difference experiences a slight uptick as the fin thickness increases. Specifically, as the fin thickness increases from 1 mm to 4 mm, the temperature difference rises from 2.31 K to 2.39 K in Case 1 and from 3.37 K to 3.62 K in Case 2. Combined with Fig. 6, it can be concluded that compared to the fin thickness, the increase in heat transfer area resulting from adjustments in fin length is more responsive to heat transfer enhancement of the fin framework. Besides, it is worth noting that for all configurations, Case 1 consistently demonstrates lower maximum temperatures and temperature differences than Case 2.

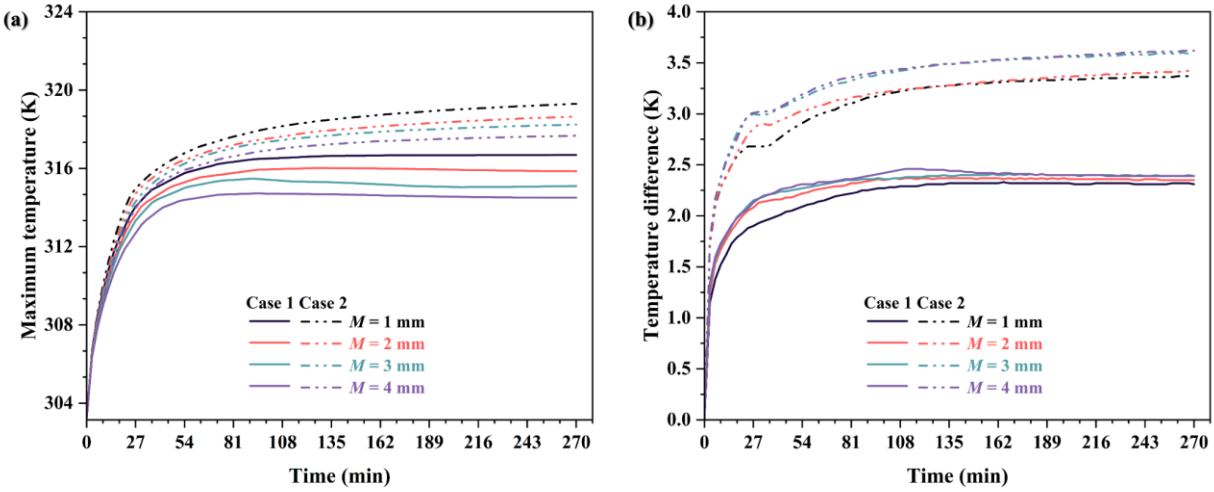

Fig. 9. Effect of fin thickness. (a) Maximum temperature; (b) Temperature difference.

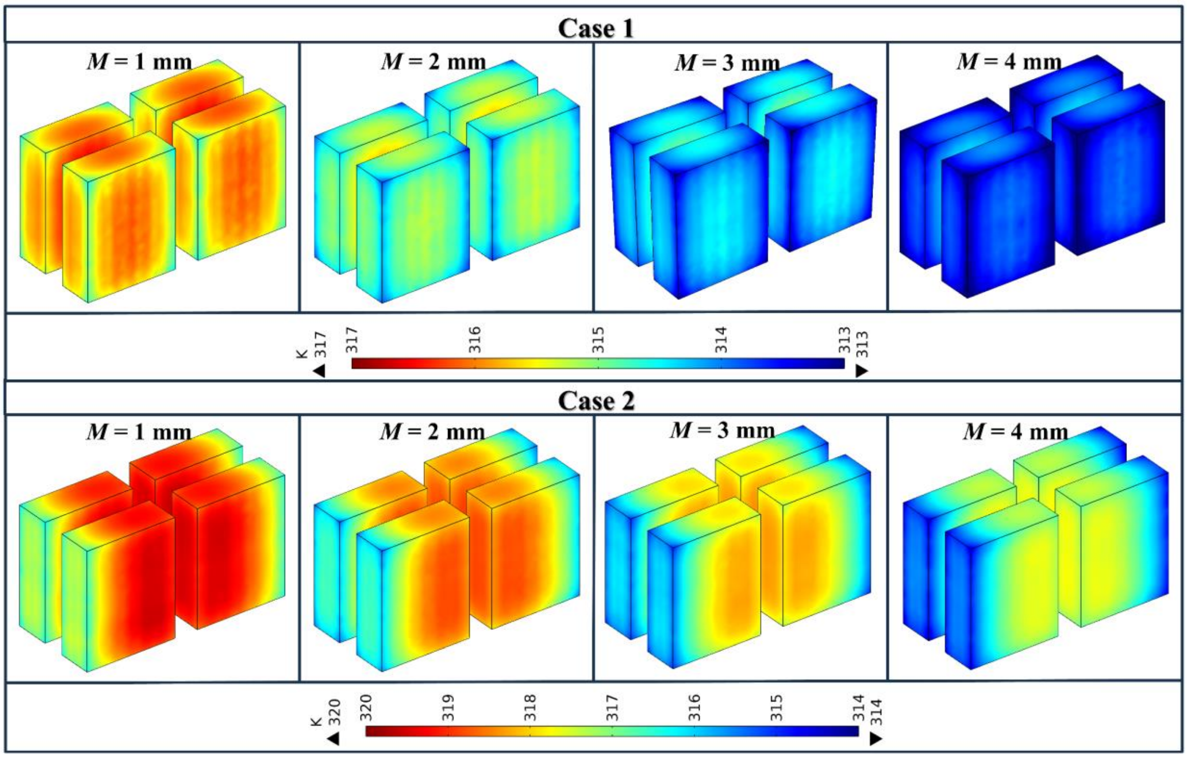

Fig. 10. Contours of the battery pack temperature distribution under different fin thicknesses at 270 min.

Fig. 10 gives the battery pack temperature distribution contours at 270 min. With the increase in fin thickness, the high-temperature range of the battery pack is immensely relieved, and the battery pack exhibits a greater temperature uniformity. Case 2 enables a higher temperature and a larger high-temperature range in the battery pack compared to Case 1. This variance can be attributed to the fewer

TECs and greater distance from the battery pack to the TEC within Case 2.

The liquid fraction of PCMs under different fin thicknesses is illustrated in Fig. 11(a). As the thickness of the fin increases, there is a decrease in the liquid fraction of the PCM. In Case 1, when discharging up to 270 min with a fin thickness of 1 mm, the liquid fraction of PCMs is 0.039, while the PCM remains largely solidified when the fin thickness is increased to 3 mm and above. Besides, the liquid fraction of PCMs in Case 2 is quite greater than that in Case 1, due to the fewer TECs and greater distance from the battery pack to the TEC. Fig. 11(b) illustrates the liquid fraction contours of PCMs at 270 min. With an increase in fin thickness, the melting region of the PCM gradually diminishes. In Case 1, only a small amount of PCMs near the battery area undergoes melting, while in Case 2, a significant portion is melted. Apparently, Case 1 exhibits a better thermal performance than Case 2.

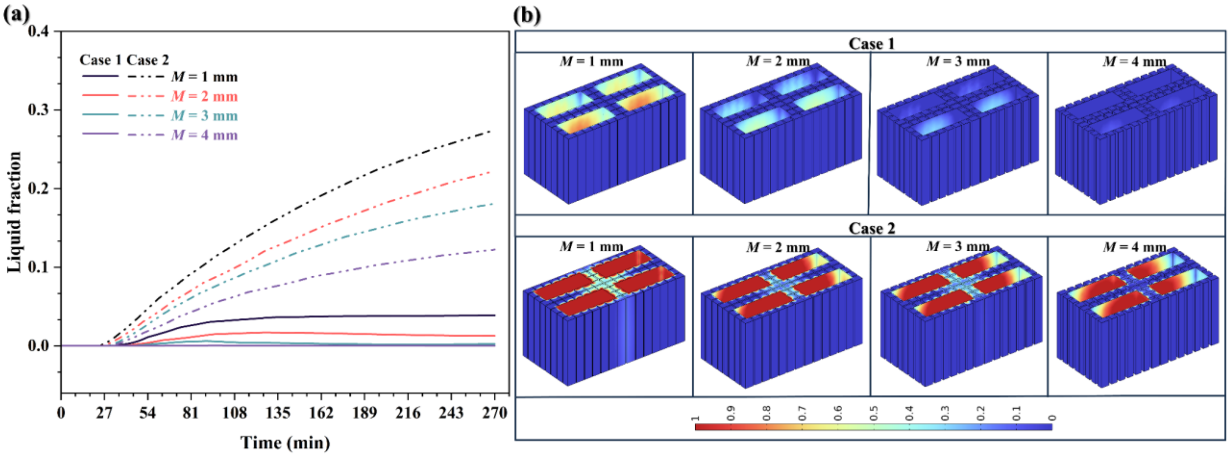

Fig. 11. Liquid fraction of PCMs at different fin thicknesses. (a) The change of liquid fraction of PCMs during battery discharge; (b) Liquid fraction distribution contours of PCMs at 270 min.

Based on the above analysis, the temperature difference of batteries at the fin thickness of 4 mm is slightly higher than that at the fin thickness of 3 mm. Although the increase of fin thickness can further reduce the maximum temperature and alleviate the melting of PCMs, it will deteriorate the temperature difference and increase the system weight as well. Consequently, the optimal fin thickness of 3 mm is suggested.

4.4 Effect of the TEC input current

An extremely high current input can lead to a substantial increase in power consumption, while insufficient current inputs may fail to effectively regulate the temperature of the battery pack. Therefore, it is vital to investigate the effect of TEC input current on thermal performance. Herein, four different TEC input currents (2 A, 3 A, 4 A, and 5 A) are employed to perform studies while keeping the fin length at 7 mm, fin thickness at 3 mm, and battery discharge rate at 3 C. Furthermore, with an increase in the input current, the temperature difference between the two ends of the TEC also experiences an increase, and the increased temperature differential deteriorates the cooling efficiency of the TEC. Consequently, an S-shaped liquid cooling plate is employed on the hot side of the TEC to lower its temperature difference.

Fig. 12(a) showcases the maximum battery temperature variation for different TEC input currents. Increasing the TEC input current leads to a higher cooling power, thus lowering the maximum temperature for both cases. The maximum temperature exhibits a significant reduction when the TEC input current is increased from 2 A to 5 A, with Case 1 experiencing a drop from 317.88 K to 309.66 K and Case 2 showing a decrease from 321.47 K to 311.38 K. Furthermore, at the same TEC input current, the maximum temperatures of Case 1 are consistently lower than those of Case 2. Significantly, even at the TEC input current of 2 A, the maximum temperature does not exceed 323.15 K for either case. The variation in temperature difference under different TEC input currents is showcased in Fig. 12(b). Due to the rapid response of the TEC, during the initial discharge phases, raising the TEC input current leads to a temperature difference increase. However, as time passes, the temperature difference alteration becomes smooth. At 270 min, when the TEC input current is raised from 2 A to 5 A, the temperature difference decreases from 3.65 K to 3.51 K for Case 1 and from 2.46 K to 2.19 K for Case 2. It is concluded that variations in current primarily impact the maximum temperature, with a limited effect on the temperature difference. Details of the battery surface temperature distribution when the battery pack is discharged for 270 min can be found in Fig. 13.

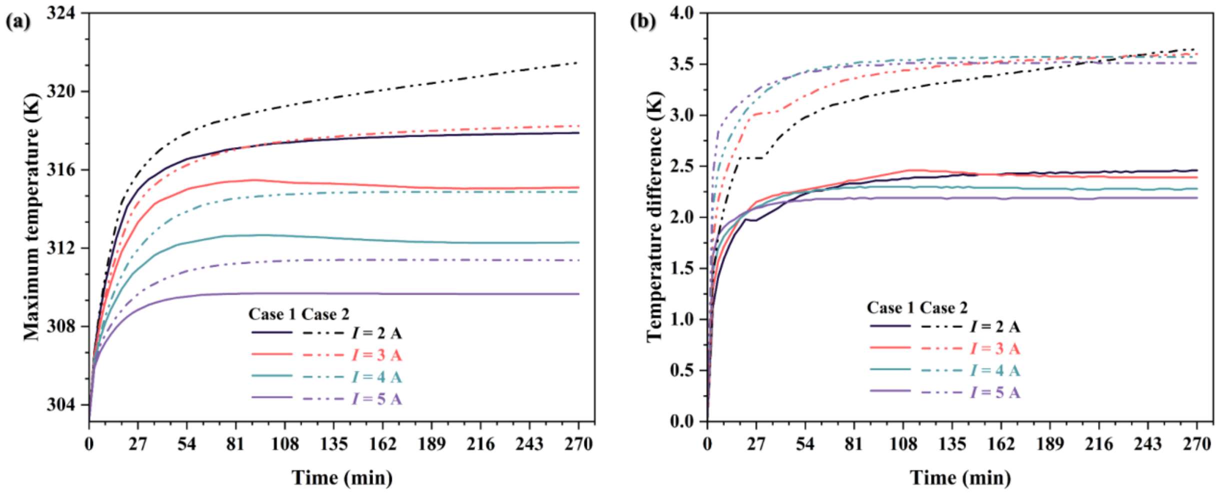

Fig. 12. Effect of the TEC input current. (a) Maximum temperature; (b) Temperature difference.

The variation of PCM liquid fraction concerning different TEC input currents is depicted in Fig. 14(a). An increase in the TEC input current results in a decrease in the PCM liquid fraction. When the

TEC input current reaches 3 A or higher in Case 1 and 4 A or higher in Case 2, the PCM does not undergo melting. At the TEC input current of 2 A, the PCM liquid fraction is 0.147 for Case 1 and 0.685 for Case 2, while they respectively decrease to 0.002 and 0.181 at the TEC input current of 3 A. Details of the liquid fraction contour of PCMs when the battery is discharged to 270 min are shown in Fig. 14(b). At a constant TEC input current of 2 A, in Case 1, only the PCM region close to the battery pack undergoes melting, whereas in Case 2, the PCM melts except for the area near the TEC. As the TEC input current rises, the extent of PCM melting progressively diminishes.

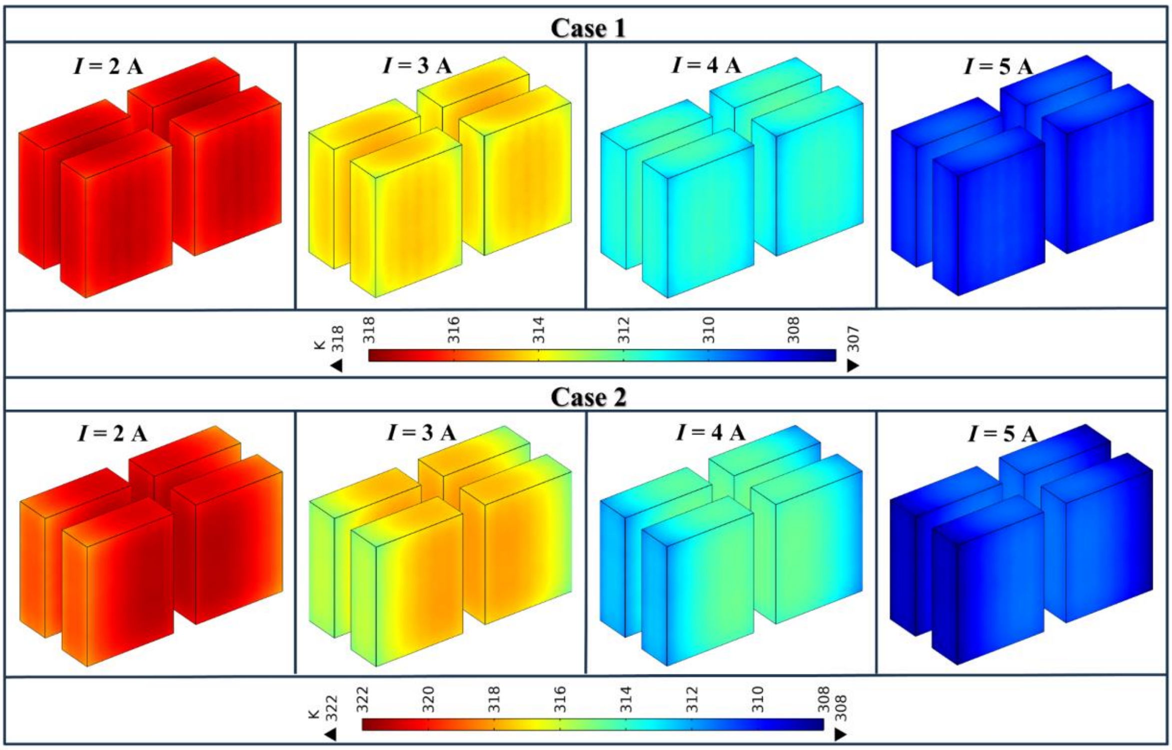

Fig. 13. Contours of the battery temperature distribution under different TEC input currents at 270 min.

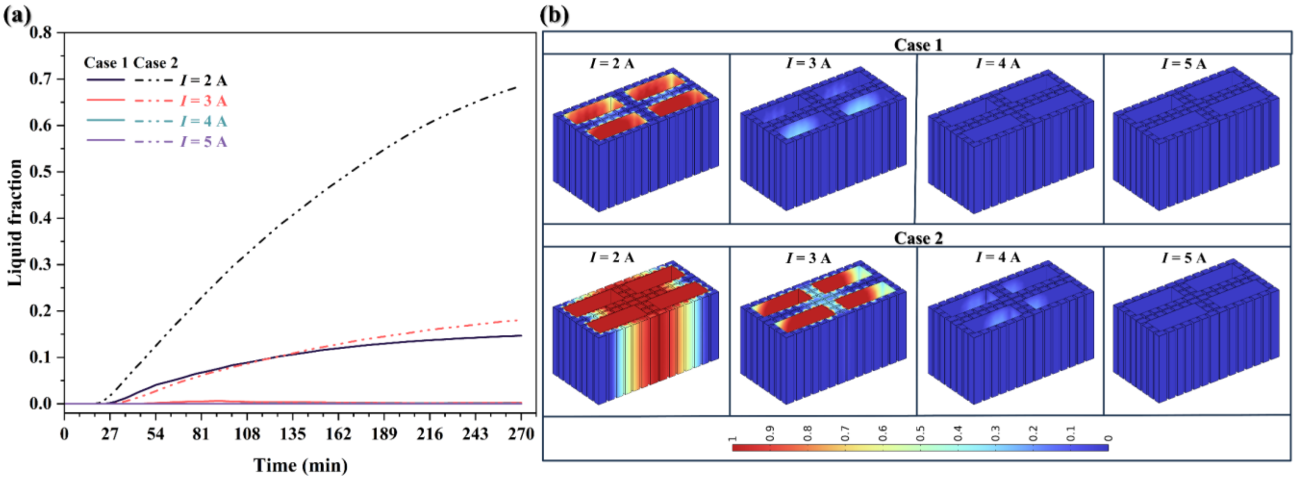

Fig. 14. Liquid fraction of the PCM at different TEC input currents. (a) The change of liquid fraction of the PCM during

battery discharge; (b) Liquid fraction distribution contours of the PCM at 270 min.

To summarize, the thermal performance of the system is effectively improved with the increase of the TEC input current. However, when the TEC input current reaches 3 A, the thermal performance of the system already meets the requirements well, and as the current further increases, the performance improvement decreases, accompanied by an increase in energy consumption. For this reason, the optimal TEC input current value of 3 A is suggested.

4.5 Effect of battery discharge rate

To comprehensively explore the exceptional performance of the BTMS, this section extends the battery discharge rate. Employing the previously mentioned optimal structure, the TEC input current is increased to 5 A to evaluate the system's performance at extreme battery discharge rates of 4 C and 5 C.

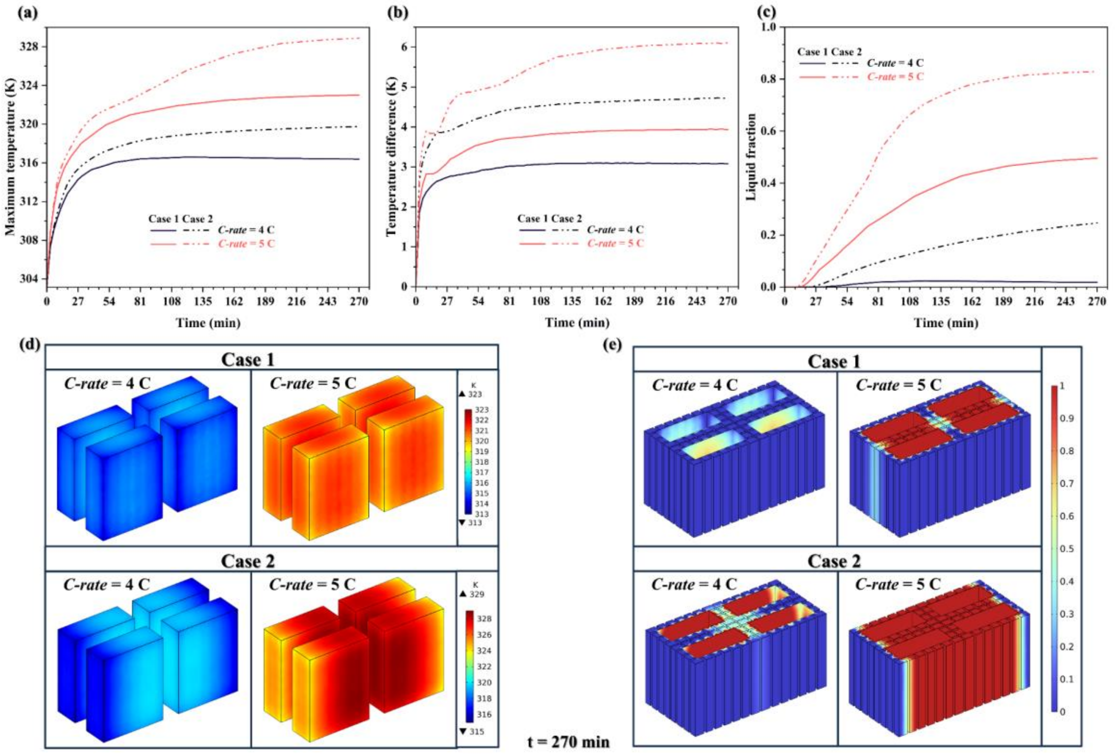

Fig. 15. Effect of different battery discharge rates. (a) Maximum temperature; (b) Temperature difference; (c) The liquid fraction of PCMs; (d) Contours of the battery pack temperature distribution at 270 min; (e) Liquid fraction distribution contours of PCMs at 270 min.

Figs 15(a), (b), and (c) display the maximum temperature, temperature difference, and PCM liquid fraction with discharge time for different discharge rates, respectively. The increase in the battery discharge rate leads to increased values for maximum temperature, temperature difference, and PCM liquid fraction in both cases. Under a discharge rate of 4 C, Case 1 exhibits a maximum temperature of 316.39 K, a temperature difference of 3.08 K, and a PCM liquid fraction of 0.018. Meanwhile, for Case 2, these values are 319.75 K, 3.94 K, and 0.246, respectively. Upon elevating the discharge rate to 5 C, Case 1 exhibits values of 323.01 K for maximum temperature, 4.72 K for temperature difference, and 0.496 for the liquid fraction of PCMs. Meanwhile, for Case 2, these values are 328.89 K, 6.11 K, and 0.829. More about the temperature distribution contours of batteries when discharged for up to 270 min can be found in Fig. 15(d). It can be found that the area of the high-temperature region in Case 2 is significantly higher than that in Case 1 in the same situation. Fig. 15(e) shows the liquid fraction contour of PCMs at 270 min. In Case 1, with a discharge rate of 4 C, it is evident that the PCM remains largely unmelted. However, when the discharge rate is elevated to 5 C, the portion of the PCM situated far from the TEC begins to melt. In Case 2, with a discharge rate of 4 C, the PCM in direct proximity to the battery pack has melted, whereas as the discharge rate is further raised to 5 C, all PCMs reach a state of melting.

From the above description, it is evident that at a discharge rate of 4 C, both cases successfully keep the maximum temperature below 323.15 K and the temperature difference below 5 K. Moreover, the melting of the PCM is effectively controlled. In the event of a battery discharge rate of 5 C, Case 2 slightly exceeds the temperature limit with regards to maximum temperature and temperature difference, while Case 1 stays within the desired range. It is noteworthy that sustained discharge at a high rate of 5 C is not frequently encountered in everyday usage. Therefore, both cases showcase outstanding performance even at this elevated discharge rate.

5. Conclusions

In this work, a BTMS integrated with TECs and PCMs is developed to ensure the temperature working environment of batteries. The system applies a stacked design, which can be extended to achieve wider applications. Meanwhile, in response to the challenge of a rapid increase in battery temperature and temperature difference due to excessive PCM melting after long charging and discharging cycles, a novel fin framework is employed to enhance the heat transfer among the TEC, battery, and PCM. To obtain the optimal fin parameters and analyze the thermal performance of the BTMS, a transient thermal-electric-fluid multi-physical field numerical model is established. The key findings are outlined below:

(1) The configuration in Case 1 is more favorable compared to the one in Case 2, due to the fewer TECs and greater distance from the battery pack to the TEC within Case 2. Under the optimal fin

parameters, both cases are able to adhere to the battery temperature requirements, except for Case 2 wherein the maximum temperature and temperature difference exceed the limit values at an ultrahigh discharge rate of 5 C.

(2) Compared to fin thickness, fin length has a more significant impact on the system thermal performance. The maximum temperature, temperature difference, and PCM liquid fraction decrease with an increase in both fin length and thickness, with a tiny influence of temperature difference by the fin thickness. The optimal fin framework with the fin length of 7 mm and fin thickness of 3 mm enables the BTMS to effectively control the melting of PCM and the battery temperature even for a stable state after long charging and discharging cycles.

(3) Increasing the TEC input current will result in a decrease in the maximum temperature and PCM liquid fraction, with minimal impact on the temperature difference. At a 3 C discharge rate, the optimal TEC input current of 3 A is obtained, with the maximum temperature, temperature difference, and PCM liquid fraction of 315.10 K, 2.39 K, and 0.002, respectively for Case 1, and 318.24 K, 3.60 K, and 0.181, respectively for Case 2.

(4) When the battery discharge rate increases, the TEC input current should also increase accordingly to ensure the battery's temperature performance. At a high discharge rate of 5 C, the BTMS configuration in Case 1 can maintain the optimal battery operating temperature environment with a TEC input current of 5 A, while the maximum temperature and temperature difference in Case 2 exceed the limits.

(5) In future studies, we will further optimize the parameters of the TEC to improve the thermal performance of the BTMS. In addition, we will comprehensively consider the thermal performance and overall energy consumption of the BTMS, and explore a control strategy to achieve dynamic temperature regulation under actual conditions.

Acknowledgements

This work was supported by the National Natural Science Foundation of China (Grant Nos. 52306017, U20A20301, 52250273), and the Natural Science Foundation of Hubei Province (No. 2023AFB093).

References

Babu Sanker, S., Baby, R., 2022. Phase change material based thermal management of lithium ion batteries: A review on thermal performance of various thermal conductivity enhancers. J. Energy Storage 50, 104606.

Cao, X., Zhang, N., Yuan, Y., Luo, X., 2020. Thermal performance of triplex-tube latent heat storage exchanger: simultaneous heat storage and hot water supply via condensation heat recovery. Renew. Energy 157, 616-625.

Fu, J., Tang, Y., Li, J., Ma, Y., Chen, W., Li, H., 2016. Four kinds of the two-equation turbulence model's research on flow field simulation performance of DPF's porous media and swirl-type regeneration burner. Appl. Therm. Eng. 93, 397-404.

Heyhat, M.M., Mousavi, S., Siavashi, M., 2020. Battery thermal management with thermal energy storage composites of PCM, metal foam, fin and nanoparticle. J. Energy Storage 28, 101235.

Hu, Q., Luo, D., Guo, J., Qiu, W., Wu, X., Yang, L., Wang, Z., Cui, X., Tang, J., 2023. Broad Temperature Plateau for High Thermoelectric Properties of n-Type Bi2Te2.7Se0.3 by 3D Printing-Driven Defect Engineering. ACS Appl. Mat. Interfaces 15(1), 1296-1304.

Jiang, L., Zhang, H., Li, J., Xia, P., 2019. Thermal performance of a cylindrical battery module impregnated with PCM composite based on thermoelectric cooling. Energy 188, 116048.

Li, B., Mao, Z., Song, B., Wang, Y.-F., Tian, W., Lu, C., Li, M., 2023. Performance evaluation and heat transfer mechanism for battery thermal management of autonomous underwater vehicles based on phase change material cooling. Appl. Therm. Eng. 219, 119655.

Li, M., Ma, S., Jin, H., Wang, R., Jiang, Y., 2023. Performance analysis of liquid cooling battery thermal management system in different cooling cases. J. Energy Storage 72, 108651.

Li, W.Q., Qu, Z.G., He, Y.L., Tao, Y.B., 2014. Experimental study of a passive thermal management system for high-powered lithium ion batteries using porous metal foam saturated with phase change materials. J. Power Sources 255, 9-15.

Lin, S., Zhou, L., 2023. Thermal performance of rectangular serpentine mini-channel cooling system on lithium battery. J. Clean. Prod. 418, 138125.

Ling, Z., Li, S., Cai, C., Lin, S., Fang, X., Zhang, Z., 2021. Battery thermal management based on multiscale encapsulated inorganic phase change material of high stability. Appl. Therm. Eng. 193, 117002.

Liu, X., Zhang, C.-F., Zhou, J.-G., Xiong, X., Wang, Y.-P., 2022. Thermal performance of battery thermal management system using fins to enhance the combination of thermoelectric Cooler and phase change Material. Appl. Energy 322, 119503.

Liu, Z., Liu, Z., Liu, J., Wang, N., 2023. Thermal management with fast temperature convergence based on optimized fuzzy PID algorithm for electric vehicle battery. Appl. Energy 352, 121936.

Luo, D., Li, Y., Yan, Y., Hu, X., Fan, X.a., Chen, W.-H., Ren, Y., Cao, B., 2023a. Realizing ultrahigh ZT value and efficiency of the Bi2Te3 thermoelectric module by periodic heating. Energy Convers. Manag. 296, 117669.

Luo, D., Yan, Y., Chen, W.-H., Yang, X., Chen, H., Cao, B., Zhao, Y., 2023b. A comprehensive hybrid transient CFD-thermal resistance model for automobile thermoelectric generators. Int. J. Heat Mass Transfer 211, 124203.

Luo, D., Yan, Y., Li, Y., Wang, R., Cheng, S., Yang, X., Ji, D., 2023c. A hybrid transient CFD-thermoelectric numerical model for automobile thermoelectric generator systems. Appl. Energy 332, 120502.

Luo, D., Yan, Y., Li, Y., Yang, X., Chen, H., 2023d. Exhaust channel optimization of the automobile thermoelectric generator to produce the highest net power. Energy 281, 128319.

Luo, J., Gu, H., Xu, X., Huang, L., Zou, D., 2023. Development of a pipeless, cascade phase change power battery thermal management system. J. Clean. Prod. 423, 138797.

Mousavi, S., Zadehkabir, A., Siavashi, M., Yang, X., 2023. An improved hybrid thermal management system for prismatic Li-ion batteries integrated with mini-channel and phase change materials. Appl. Energy 334, 120643.

Peng, P., Wang, Y., Jiang, F., 2022. Numerical study of PCM thermal behavior of a novel PCM-heat pipe combined system for Li-ion battery thermal management. Appl. Therm. Eng. 209, 118293.

Ranjbaran, Y.S., Shojaeefard, M.H., Molaeimanesh, G.R., 2023. Thermal performance enhancement of a passive battery thermal management system based on phase change material using cold air passageways for lithium batteries. J. Energy Storage 68, 107744.

Sait, H., 2022. Cooling a plate lithium-ion battery using a thermoelectric system and evaluating the geometrical impact on the performance of heatsink connected to the system. J. Energy Storage 52, 104692.

Shan, S., Li, L., Xu, Q., Ling, L., Xie, Y., Wang, H., Zheng, K., Zhang, L., Bei, S., 2023. Numerical investigation of a compact and lightweight thermal management system with axially mounted cooling tubes for cylindrical lithium-ion battery module. Energy 274, 127410.

Siddique, A.R.M., Mahmud, S., Heyst, B.V., 2018. A comprehensive review on a passive (phase change materials) and an active (thermoelectric cooler) battery thermal management system and their limitations. J. Power Sources 401, 224-237.

Singh, L.K., Kumar, R., Gupta, A.K., Sharma, A.K., Panchal, S., 2023. Computational study on hybrid air-PCM cooling inside lithium-ion battery packs with varying number of cells. J. Energy Storage 67, 107649.

Song, W., Bai, F., Chen, M., Lin, S., Feng, Z., Li, Y., 2018. Thermal management of standby battery for outdoor base station based on the semiconductor thermoelectric device and phase change materials. Appl. Therm. Eng. 137, 203-217.

Subramanian, M., Hoang, A.T., B, K., Nižetić, S., Solomon, J.M., Balasubramanian, D., C, S., G, T., Metghalchi, H., Nguyen, X.P., 2021. A technical review on composite phase change material based secondary assisted battery thermal management system for electric vehicles. J. Clean. Prod. 322, 129079.

Talele, V., Zhao, P., 2023. Effect of nano-enhanced phase change material on the thermal management of a 18650 NMC battery pack. J. Energy Storage 64, 107068.

Tang, J., Ni, H., Peng, R.-L., Wang, N., Zuo, L., 2023. A review on energy conversion using hybrid photovoltaic and thermoelectric systems. J. Power Sources 562, 232785.

Weng, J., Huang, Q., Li, X., Zhang, G., Ouyang, D., Chen, M., Yuen, A.C.Y., Li, A., Lee, E.W.M., Yang, W., Wang, J., Yang, X., 2022. Safety issue on PCM-based battery thermal management: Material thermal stability and system hazard mitigation. Energy Storage Mater. 53, 580-612.

Wu, W., Wu, W., Wang, S., 2018. Thermal management optimization of a prismatic battery with shape-stabilized phase change material. Int. J. Heat Mass Transfer 121, 967-977.

Yang, H., Li, M., Wang, Z., Ma, B., 2023. A compact and lightweight hybrid liquid cooling system coupling with Z-type cold plates and PCM composite for battery thermal management. Energy 263, 126026.

Zhang, F., Lu, F., Liang, B., Zhu, Y., Gou, H., Xiao, K., He, Y., 2023. Thermal performance analysis of a new type of branch-fin enhanced battery thermal management PCM module. Renew. Energy 206, 1049-1063.

Zhang, F., Zhai, L., Zhang, L., Yi, M., Du, B., Li, S., 2022. A novel hybrid battery thermal management system with fins added on and between liquid cooling channels in composite phase change materials. Appl. Therm. Eng. 207, 118198.

Zhang, W., Liang, Z., Yin, X., Ling, G., 2021. Avoiding thermal runaway propagation of lithium-ion battery modules by using hybrid phase change material and liquid cooling. Appl. Therm. Eng. 184, 116380.

Zhang, Y., Tavakoli, F., Abidi, A., Li, Z., Aybar, H.Ş., Heidarshenas, B., 2022. Investigation of horizontal and vertical distance of lithium-ion batteries on the thermal management of the battery pack filled with phase change material with the air flow. J. Power Sources 550, 232145.